catalysts

MDPI

Article

Ni(II)–Aniline Complex-Modified TiO_2 as a Bifunctional Electrocatalyst for Enhanced Hydrogen and Oxygen Evolution in Alkaline Water Splitting

Jayaraj Sekar [1], Meera Naachiyar Ramadhasan [2], Elayaraja Sakthivel [1], Rajkumar Kanniah [3], Ganeshraja Ayyakannu Sundaram [1,*] and Junhu Wang [4,*]

[1] Energy and Environmental Nanomaterials Laboratory (E^2Nano Lab), Department of Research Analytics, Saveetha Dental College and Hospitals, Saveetha Institute of Medical and Technical Sciences, Poonamallee High Road, Chennai 600077, Tamil Nadu, India; jaichemistry10@gmail.com (J.S.)
[2] Centre for Green Hydrogen and Carbon Neutral Technologies, Department of Physics, Karpagam Academy of Higher Education, Coimbatore 641021, Tamil Nadu, India; meeranaachiyarr.physics@gmail.com
[3] Department of Chemistry, Saveetha Institute of Natural and Physical Sciences (SINAPS), Saveetha Institute of Medical and Technical Sciences (SIMATS), Thandalam, Chennai 602105, Tamil Nadu, India; rajkumark.sse@saveetha.com
[4] Mössbauer Effect Data Center, CAS Key Laboratory of Science and Technology on Applied Catalysis, Dalian Institute of Chemical Physics, Chinese Academy of Sciences, Dalian 116023, China
* Correspondence: ganeshrajaas.sdc@saveetha.com or asgchem84@gmail.com (G.A.S.); wangjh@dicp.ac.cn (J.W.)

Abstract

Developing cost-effective bifunctional electrocatalysts for alkaline water splitting is essential for sustainable hydrogen production. Herein, Ni(II)–aniline complex-modified TiO_2 (Ni–TiO_2) nanoparticles were synthesized via a simple surface-modification strategy and evaluated for the hydrogen evolution reaction (HER) and oxygen evolution reaction (OER) in 1 M KOH. X-ray diffraction and Raman spectroscopy confirmed the retention of the anatase TiO_2 structure without detectable crystalline nickel-containing secondary phases. Surface characterization of Ni–TiO_2 nanoparticles before and after OER testing was performed using FE-SEM and EDX. X-ray photoelectron spectroscopy revealed predominantly Ti^{4+} and surface-associated Ni^{2+} species, while optical and photoluminescence analyses indicated modifications to the optical and interfacial properties of TiO_2. Ni–TiO_2 exhibited improved HER activity, requiring overpotentials of 267.2 and 373.1 mV at current densities of 10 and 50 mA cm^{-2}, respectively, compared with 317.3 and 462.2 mV for pristine TiO_2. Its lower Tafel slope (126.5 versus 163.79 mV dec^{-1}) and higher electrochemically active surface area (142.25 versus 5.87 cm^2) further indicated improved reaction kinetics and surface accessibility. Ni–TiO_2 retained 92.55% of its initial HER activity after 12 h at 100 mA cm^{-2}. For OER, it achieved 50 mA cm^{-2} at an overpotential of 381.3 mV, compared with 500.6 mV for pristine TiO_2, and exhibited a lower Tafel slope (86.7 versus 143.4 mV dec^{-1}). The catalyst maintained 88.2% of its initial OER current after 12 h at 50 mA cm^{-2}. These findings demonstrate that Ni(II)–aniline modification improves the electrocatalytic activity and operational stability of TiO_2 toward both HER and OER, highlighting its potential as a coordination-chemistry-assisted strategy for alkaline water splitting.

Keywords: Ni(II)–aniline complex; TiO_2 nanomaterials; hydrogen evolution reaction (HER); oxygen evolution reaction (OER); alkaline water splitting

Check for updates

Academic Editor: Edward G. Gillan

Received: 18 September 2026
Revised: 1 November 2026
Accepted: 3 November 2026
Published: 6 November 2026

Copyright: © 2026 by the authors. Licensee MDPI, Basel, Switzerland. This article is an open access article distributed under the terms and conditions of the Creative Commons Attribution (CC BY) license.

1. Introduction

The growing demand for sustainable and low-carbon energy technologies has intensified interest in green hydrogen as a versatile energy carrier for energy storage, transportation, chemical production, and renewable-energy integration. Among hydrogen-production technologies, renewable-electricity-driven water electrolysis is particularly attractive because it converts electrical energy into chemical energy without direct carbon emissions. Recent advances in electrocatalyst design have demonstrated the potential of composition and electronic-structure engineering to improve water-splitting performance [1–4]. Alkaline water electrolysis (AWE) is especially promising for large-scale hydrogen production owing to its technological maturity, relatively low-cost electrolyte, and compatibility with earth-abundant catalysts [5–7]. However, its efficiency is largely governed by the kinetics of the hydrogen evolution reaction (HER) at the cathode and the oxygen evolution reaction (OER) at the anode. The OER is particularly challenging because it involves multiple proton-coupled electron-transfer steps and O–O bond formation, resulting in substantial kinetic barriers and energy losses. Recent studies have demonstrated improved alkaline water-splitting activity through interfacial and electronic-structure engineering, while emerging research has highlighted the importance of dynamic electrode–reactant interactions in governing electrocatalytic performance [2,8,9]. Consequently, developing highly active, durable, and economically viable electrocatalysts for both HER and OER remains a major research priority. Current strategies increasingly focus on tailoring catalyst composition, electronic structure, surface chemistry, interfaces, and active-site environments to overcome these kinetic limitations and improve overall water-splitting efficiency [2,8–10].

The use of noble-metal catalysts alongside earth-abundant transition-metal-based materials is vital for the practical expansion of cost-effective alkaline electrolyzers [6]. In this framework, Ni-, Fe-, Co-, and Mn-containing materials, including metals, oxides, hydroxides, alloys, phosphides, sulfides, spinels, and heterostructures, have received extensive attention. Among these elements, nickel is mainly attractive because of its earth abundance, relatively low cost, corrosion resistance in alkaline media, and flexible redox chemistry. Ni-based materials are particularly applicable to OER, where surface oxidation and the formation of higher-valence NiOOH-like species under anodic polarization are closely related to catalytic activity [11]. Together, nickel-based materials have established promising HER activity in alkaline media, where effective water dissociation and subsequent hydrogen-intermediate formation are important kinetic considerations. Recent comprehensive studies have highlighted that the activity and durability of Ni-based electrocatalysts can be considerably improved through alloying, heteroatom incorporation, defect engineering, interface construction, nanostructuring, and electronic-structure modulation [9,12,13]. Additionally, the local coordination and electronic environment surrounding Ni centers are progressively recognized as imperative parameters for controlling electrocatalytic reaction pathways [12].

Elsewhere, conservative compositional modification and molecular and coordination-chemistry methodologies offer an alternate strategy for controlling the local electronic structure of transition-metal catalytic centers. In particular, the ligand environment surrounding Ni(II) can impact its oxidation state, charge distribution, coordination geometry, redox characteristics, and interface with reaction intermediates. Recent studies have established that molecular Ni(II) complexes can function as electrocatalysts for hydrogen evolution, with catalytic behaviour strongly influenced by ligand structure and the electronic properties of the coordination sphere. For instance, Ni(II) complexes containing thiosemicarbazone ligands have been revealed to catalyse HER, whereas recent studies of Ni(II) phosphine and imine complexes have further demonstrated the potential of coordination-defined nickel centers for electrochemical hydrogen generation [14–16]. These developments indicate that rational control of the Ni coordination environment represents a promising route for tuning

catalytic behaviour beyond conventional metal, oxide, or alloy compositions. Similarly, Ni(II)-based coordination polymers have recently been reported to exhibit electrocatalytic activity toward both HER and OER in alkaline electrolyte, further supporting the relevance of coordination chemistry to bifunctional water-splitting catalysis [17,18].

Incidentally, aniline is an exciting nitrogen-containing ligand for modifying the local chemical environment of Ni(II). The existence of an amino group offers a coordination site capable of interacting with Ni(II), although the aromatic framework can stimulate the electronic environment and interfacial characteristics of the resulting hybrid material. Notably, previous work has established that aniline-derived surface alteration can significantly influence the HER behaviour of nickel electrodes. Electropolymerized aniline on Ni electrodes was stated to distinctly enhance alkaline HER performance and stability, demonstrating that nitrogen-containing organic environments can constructively modify the electrochemical behaviour of nickel-based catalytic surfaces [19]. While this study involved an electropolymerized aniline layer rather than a distinct Ni(II)–aniline coordination structure, it offers an important theoretical basis for developing aniline-mediated modification of Ni-containing electrocatalysts. Conversely, the considered incorporation of a Ni(II)–aniline coordination environment onto TiO_2 for synchronized HER and OER has, to the best of our knowledge, been established very limited in the literature. Such a method could afford a distinct means of participating coordination chemistry with an inorganic oxide framework for monitoring catalytic-site environment and interfacial electronic properties [20].

Titanium dioxide (TiO_2) represents a convincing inorganic platform for the engineering of hybrid electrocatalysts due to its excellent chemical robustness, structural versatility, tunable surface chemistry, rich defect landscape, and strong interfacial affinity toward transition-metal species [21]. However, pristine TiO_2 normally shows essentially modest electrocatalytic activity, primarily owing to its limited electronic conductivity and consequently sluggish interfacial charge-transport characteristics. Intentional physicochemical modulation of the TiO_2 lattice, through compositional tailoring, defect-state engineering, morphological regulation, and deliberate building of heterointerfaces, can effectively manipulate its electronic structure, surface energetics, and charge-transfer characteristics, thus substantially augmenting its electrochemical functionality [22]. A recent comprehensive review highlighted the growing application of TiO_2-based nanostructures in HER, OER, and other redox reactions, highlighting the roles of surface states, morphology, interfaces, charge transport, and active-site convenience in determining catalytic behaviour [22]. Significantly, TiO_2 should not be considered an electronically passive support. Recent studies have shown that TiO_2 can significantly influence the structural evolution, stability, and electronic environment of Ni-containing electrocatalysts. For example, a TiO_2-supported NiFe precursor showed enhanced OER activity and durability in 1.0 M KOH, with in situ Raman and infrared studies representing the dynamic transformation of the Ni-containing phase toward catalytically active NiOOH species during OER [23]. Likewise, TiO_2-supported NiFeMo oxide systems have established enhanced OER activity and stability, with TiO_2 contributing to the stabilization of the catalyst under highly oxidative conditions and influencing the formation of catalytically active Ni/Fe oxyhydroxide species [24]. These results establish TiO_2 as a potentially functional constituent for regulating the electrochemical properties of nickel-containing catalytic interfaces.

The arrangement of a coordination-defined Ni(II) center, aniline ligand, and TiO_2 hence offers an exciting platform for simultaneously manipulating chemical coordination, electronic structure, and oxide–metal interfacial interactions [25]. In such a hybrid system, TiO_2 may afford a structurally stable inorganic context, while the Ni(II) center can serve as a redox-active catalytic component and the coordinated aniline ligand may modulate the local electronic environment of Ni. The ensuing interfacial interaction could influence charge-

transfer characteristics, hydroxide/water activation, adsorption of reaction intermediates, and the availability of catalytically relevant surface sites. These factors are predominantly important for alkaline HER, where water activation and hydrogen adsorption/desorption are central to the reaction kinetics, and for OER, where the generation and evolution of higher-valence Ni oxyhydroxide species are intensely correlated to catalytic activity [9,12,23]. Recent studies on the local regulation of nickel-based catalysts additionally highlight that controlling the electronic and coordination environment of Ni is an operative strategy for improving water-splitting performance and stability [12,13,26].

Although there has been substantial progress in Ni-based electrocatalysts, Ni(II) coordination chemistry, and TiO_2-containing catalytic interfaces, the incorporation of a Ni(II)–aniline coordination environment with TiO_2 for bifunctional alkaline water splitting remains inadequately explored. Specifically, the relationship between the structural and electronic modifications encouraged by Ni(II)–aniline coordination and the resulting HER/OER activity has not been methodically established. Addressing this gap involves comprehensive characterization of the structural, vibrational, optical, morphological, and surface-electronic properties of the hybrid material together with relative electrochemical evaluation against pristine TiO_2 [27,28].

In the current work, we report the preparation of a Ni(II)–aniline complex-modified TiO_2 (Ni–TiO_2) hybrid electrocatalyst and thoroughly examine its physicochemical and electrocatalytic properties. The structural and electronic characteristics of the prepared material were widely observed using X-ray diffraction (XRD), Fourier-transform infrared (FTIR) spectroscopy, Raman spectroscopy, diffuse reflectance spectroscopy (DRS), photoluminescence (PL), field-emission scanning electron microscopy (FE-SEM) coupled with energy-dispersive X-ray (EDX) spectroscopy, and X-ray photoelectron spectroscopy (XPS). The electrocatalytic performance of Ni–TiO_2 was assessed toward HER and OER in 1 M KOH using TiO_2 as the orientation material. Electrochemical measurements—including cyclic voltammetry, polarization analysis, electrochemical double-layer capacitance, and stability testing—were conducted to measure the influence of Ni(II)–aniline modification on the electrochemically accessible surface characteristics, catalytic kinetics, and durability of TiO_2. Specific importance is placed on relating the spectroscopic and surface-chemical characteristics of Ni–TiO_2 with its improved bifunctional electrocatalytic performance.

Overall, this study presents a coordination-chemistry-assisted approach for the functional modification of TiO_2 with a Ni(II)–aniline complex and affords a structure–property–activity outlook for alkaline HER and OER electrocatalysis. The integration of a redox-active Ni(II) coordination environment with a steady TiO_2 framework characterizes a hypothetically useful method for evolving earth-abundant hybrid electrocatalysts for sustainable water splitting.

2. Results and Discussion

2.1. X-Ray Diffraction Analysis

The crystalline structures of pristine TiO_2 and Ni–TiO_2 were examined by X-ray diffraction (XRD), and the corresponding patterns are presented in Figure 1. Both samples show a series of well-defined diffraction reflections at $2\theta = 25.4°$, 37.0°, 37.8°, 38.7°, 48.1°, 54.0°, 55.2°, 62.7°, 62.8°, 68.9°, 70.4°, 75.3°, and 76.0°. The main reflection at approximately 25.4° can be indexed to the (101) plane of tetragonal anatase TiO_2, although the reflections at 37.0°, 37.8°, and 38.7° are attributable to the (103), (004), and (112) planes, respectively. The reflections at 48.1°, 54.0°, and 55.2° correspond to the (200), (105), and (211) planes, while the high-angle reflections can be assigned to the higher-order anatase planes, including (213), (204), (116), (220), (215), and (301). The overall diffraction pattern is consequently characteristic of the tetragonal anatase phase of TiO_2 and agrees well with reported anatase

TiO_2 diffraction data [29–31]. Similar sets of reflections have been described for anatase TiO_2 and Ni-modified TiO_2 materials, confirming that the main crystalline context remains that of anatase TiO_2 [32–34].

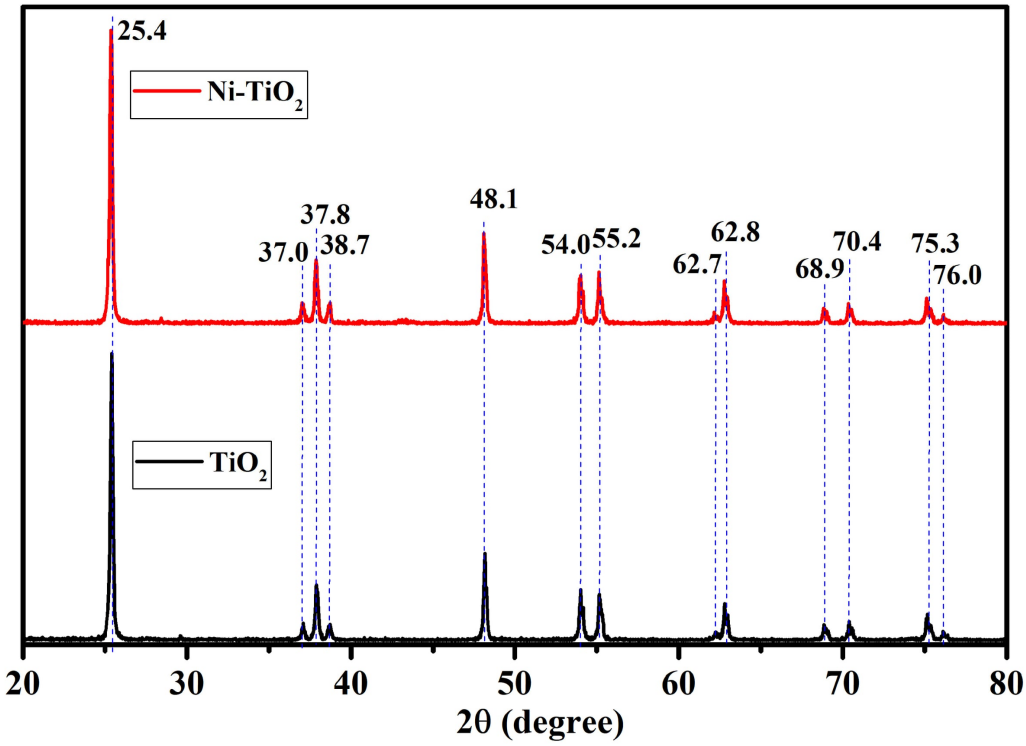


Figure 1. X-ray diffraction patterns of pristine TiO_2 and Ni–TiO_2 NPs, showing the characteristic reflections of tetragonal anatase TiO_2 and the absence of detectable additional crystalline Ni-containing phases.

A notable feature of the present results is that the XRD patterns of pristine TiO_2 and Ni–TiO_2 are closely analogous, with no measurable change in the principal TiO_2 reflections and no distinct extra diffraction peaks attributable to crystalline Ni, NiO, or other nickel-containing crystalline phases. This observation indicates that the integration of the Ni(II)–aniline complex does not induce an obvious phase transformation of the TiO_2 host structure under the preparation conditions employed. Obviously, the absence of an additional crystalline Ni-related reflection should not be interpreted as evidence for the absence of Ni. Instead, it is attributable to the low Ni loading and/or high dispersion and limited crystallinity of the Ni-containing species, for which the concentration may be below the detection sensitivity of conventional powder XRD. A similar behaviour has been stated for Ni-modified TiO_2 systems in which no distinct Ni-related reflections were observed at low Ni loading, and the presence and chemical state of Ni were then established using XPS.

The holding of the anatase structure following Ni modification is mainly important because the electrochemical properties of the resulting catalyst can then be measured in terms of surface/interface modification rather than formation of a new bulk crystalline Ti-containing phase. For Ni/TiO_2 systems, previous studies have similarly reported protection of the anatase framework, along with the absence of clearly resolved nickel-containing crystalline phases at moderately low Ni concentrations. In the present Ni–TiO_2 material, the inability to determine a separate Ni phase by XRD is hence compatible with the possibility that Ni-containing species are highly dispersed over or strongly related to the TiO_2 surface.

The close similarity of the diffraction patterns of TiO_2 and Ni–TiO_2 also suggests that the modification arises without substantial disruption of the long-range crystallographic order of TiO_2. However, because XRD principally probes long-range crystalline order, it cannot

by itself distinguish whether the Ni(II)–aniline complex is present as surface-coordinated species, highly dispersed domains, amorphous material, or low-level lattice-associated species. Therefore, the XRD results are supplemented by the Raman and XPS analyses, which offer more direct evidence regarding the chemical environment, surface interaction, morphology, and elemental/oxidation-state characteristics of Ni–TiO_2.

Overall, the XRD results confirm that the anatase TiO_2 phase remains largely preserved after Ni(II)–aniline modification, with no significant peak shifts or detectable formation of a separate crystalline nickel-containing phase. The Ni(II)–aniline complex was introduced onto the TiO_2 surface through a room-temperature adsorption method without subsequent calcination; therefore, the modification is primarily attributed to surface adsorption rather than substitutional incorporation of Ni into the TiO_2 lattice. The absence of detectable nickel-containing diffraction peaks may be attributed to the low loading, high dispersion, or poorly crystalline nature of the adsorbed species. These findings indicate that surface modification occurs without detectable disruption of the TiO_2 crystal structure, allowing the effects of Ni(II)–aniline modification on HER and OER performance to be investigated in relation to changes in surface chemistry and electronic properties rather than major bulk phase transformations. The associated surface chemical modifications were further examined using XPS and FTIR spectroscopy.

2.2. Surface Morphology and Elemental Composition of Ni–TiO_2 Nanoparticles

Figure 2a shows the FE-SEM image of the Ni–TiO_2 nanoparticles, revealing a predominantly spherical morphology with some degree of agglomeration. This aggregation may result from interparticle interactions and the tendency of nanoparticles to form clusters during drying and sample preparation. Image analysis indicated an average particle size of approximately 89 nm. The corresponding EDX spectrum (Figure 2b) revealed oxygen (47.5 at%), carbon (34.8 at%), titanium (17.4 at%), and a small amount of nickel (0.3 at%). The presence of oxygen and titanium is consistent with the TiO_2-based composition of the material, while the low nickel content suggests that Ni was present at a low detectable level in the analyzed region. The relatively high carbon content may be attributed to carbonaceous surface species, residual organic components from the synthesis, or the carbon-based substrate used during sample preparation. However, the contribution of each source cannot be distinguished from EDX analysis alone. Furthermore, the absence of a clearly detectable nitrogen signal does not provide direct evidence for the presence of aniline-derived species. Therefore, confirmation of surface modification requires complementary spectroscopic characterization, particularly FTIR, Raman, and XPS analyses.

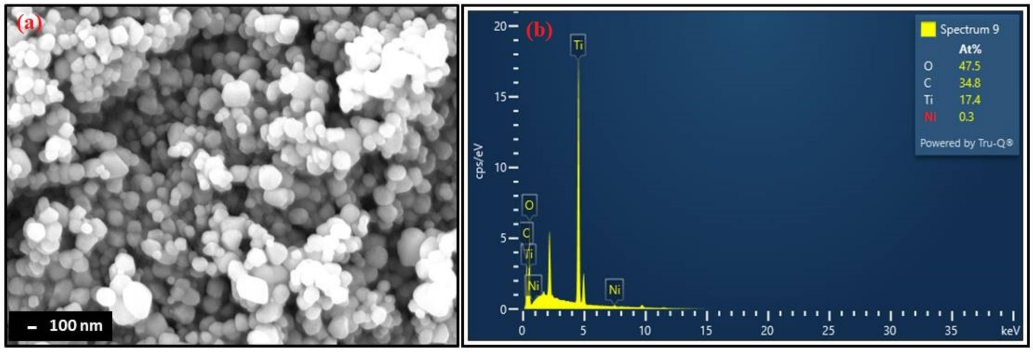


Figure 2. (**a**) FE-SEM image and (**b**) EDX image of Ni–TiO_2 NPs.

2.3. Raman and FTIR Spectroscopic Analyses

The structural and vibrational characteristics of pristine TiO_2 and Ni–TiO_2 NPs were further investigated by Raman spectroscopy, and the corresponding spectra are presented

in Figure 3a. Both TiO_2 and Ni–TiO_2 display the characteristic Raman bands of the anatase TiO_2 phase at about 143.6, 196.0, 398.4, 519.3, and 641.6 cm^{-1}. These bands can be assigned to the fundamental Raman-active modes of tetragonal anatase TiO_2—namely, the E_g mode at ~144 cm^{-1}, the E_g mode at ~197 cm^{-1}, the B_{1g} mode at ~399 cm^{-1}, the overlapping A_{1g}/B_{1g} modes near ~519 cm^{-1}, and the E_g mode at ~639 cm^{-1} [35–37]. The representative Raman modes observed here are in excellent agreement with the XRD results, indicating that the anatase phase establishes the dominant crystalline structure in both samples [31].

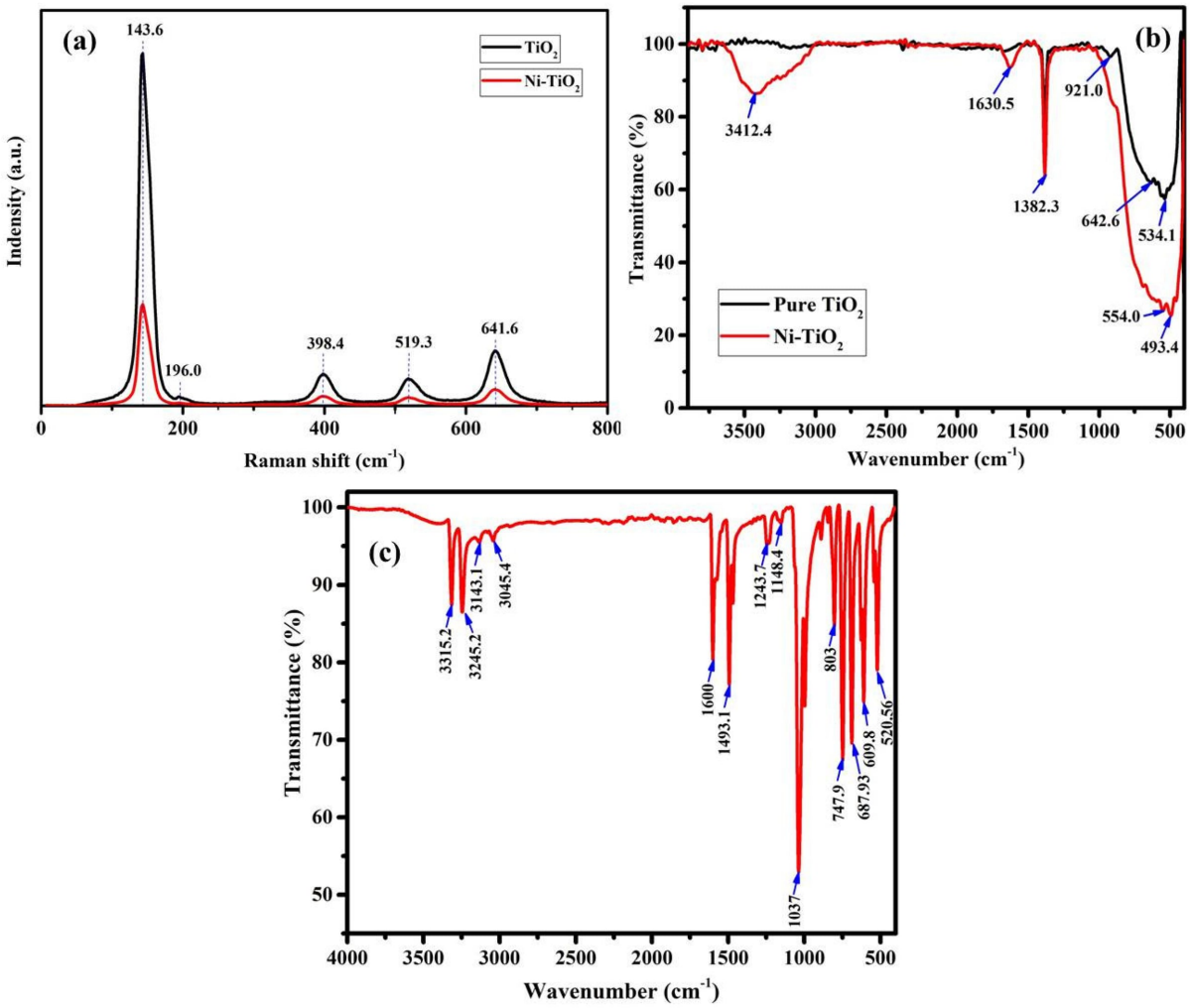


Figure 3. (**a**) Raman and (**b**) FTIR spectra of pristine TiO_2 and Ni–TiO_2 NPs, and (**c**) FTIR spectrum of $[Ni(aniline)_4Cl_2]$ complex.

A remarkable feature of Figure 3a is that the positions of the characteristic TiO_2 Raman bands remain essentially unchanged following Ni(II)–aniline modification. In particular, the intense anatase Eg mode at 143.6 cm^{-1}, together with the bands at 196.0, 398.4, 519.3, and 641.6 cm^{-1}, does not display a visible shift in Ni–TiO_2 relative to pristine TiO_2. The absence of measurable Raman shifts indicates that the modification does not produce a considerable change in the average vibrational force constants of the Ti–O framework or a considerable lattice distortion obvious by Raman spectroscopy. This remark is consistent with the XRD results, which displayed preservation of the anatase diffraction pattern without the presence of new crystalline phases. Comparable retention of anatase Raman modes without major spectral displacement has been reported for modified TiO_2 systems when the modifying species is present mainly at the surface or at relatively low concentration [38].

Although the Raman peak positions are preserved, a distinct decrease in Raman intensity is observed for Ni–TiO_2 compared with pristine TiO_2. The intensity reduction is an important spectral feature and suggests that integration of the Ni(II)–aniline complex alters the local optical/vibrational environment of the TiO_2 surface. A related study of Ni-modified TiO_2 reported a progressive decrease in the intensity of the TiO_2 Raman bands with increasing Ni loading and attributed the Raman quenching to the presence of Ni species on the TiO_2 surface, which can alter the interaction of the incident radiation with the TiO_2 nanoparticles. Such reduction in the present Ni–TiO_2 sample may similarly arise from surface-associated Ni-containing species and their interaction with TiO_2, leading to reduced effective Raman scattering from the underlying TiO_2 domains.

The absence of additional Raman bands attributable to a distinct nickel-containing crystalline phase is also notable. At the comparatively low Ni content employed in the present material, the Ni(II)–aniline species may be highly distributed and/or inadequately crystalline to generate clearly resolved Raman features. Hence, the Raman spectrum, together with the XRD pattern, does not afford evidence for the formation of a distinct bulk crystalline NiO, Ni, or other nickel oxide phase. Instead, the collective results are consistent with the presence of a surface-associated Ni(II)–aniline component on an anatase TiO_2 context.

The FTIR spectra of pure TiO_2, the parent [Ni(aniline)$_4$Cl$_2$] complex, and Ni(II)–aniline complex-modified TiO_2 nanoparticles (Ni–TiO_2 NPs) were analysed to investigate their characteristic vibrational modes and changes in the surface chemical environment. Pure TiO_2 exhibited characteristic absorption bands at 534.1 and 642.6 cm^{-1}, which are primarily attributed to Ti–O and Ti–O–Ti lattice vibrations. The band at 921.0 cm^{-1} may be associated with surface Ti–OH or other surface Ti–O vibrational modes, whereas the absorption at 1382.3 cm^{-1} can tentatively be assigned to surface-adsorbed carbonate or other carbon-containing species (Figure 3b).

The FTIR spectrum of the parent [Ni(aniline)$_4$Cl$_2$] complex (Figure 3c) provides a reference for identifying the vibrational features associated with the coordinated aniline ligands. The bands at 520.56 and 609.8 cm^{-1} may be associated with metal–nitrogen coordination-related vibrations and ligand skeletal deformations. The absorptions at 687.93, 747.9, and 803 cm^{-1} are primarily attributed to aromatic C–H out-of-plane bending vibrations. The bands at 1037 and 1148.4 cm^{-1} may arise from aromatic ring vibrations and in-plane C–H bending, while the absorption at 1243.7 cm^{-1} is consistent with C–N stretching of the aniline ligand. The bands at 1493.1 and 1600 cm^{-1} are mainly associated with aromatic ring C=C stretching and NH_2 bending vibrations, respectively. The absorption at 3045.4 cm^{-1} is attributed to aromatic C–H stretching, whereas the bands at 3143.1, 3245.2, and 3315.2 cm^{-1} fall within the N–H stretching region of the coordinated amino groups. Collectively, these vibrational features are consistent with the presence of aniline ligands in the nickel complex.

Following modification of TiO_2 with the Ni(II)–aniline complex, the low-wavenumber bands appeared at 493.4, 554.0, and 690.5 cm^{-1}, indicating changes in the local metal–oxygen vibrational environment. These changes may arise from interfacial interactions between the nickel-containing species and the TiO_2 surface. Although contributions from Ni–O or other metal–ligand vibrations cannot be excluded, these bands alone are insufficient to establish the formation of specific Ni–O bonds. Notably, the absorption at 1382.3 cm^{-1} remained observable after modification, suggesting the persistence of the associated surface species. The modified sample also exhibited additional absorptions at 1630.5 and 3412.4 cm^{-1}. The band at 1630.5 cm^{-1}, compared with the corresponding 1600 cm^{-1} feature of the parent complex, may be associated with aniline-derived NH_2 bending vibrations and/or the bending vibration of adsorbed water. Similarly, the broad absorption at 3412.4 cm^{-1} may involve

overlapping N–H and surface O–H stretching vibrations. Its position differs from the N–H stretching bands observed for the parent complex, suggesting a possible change in the local chemical environment of the amino groups following modification.

A comparison of the three spectra therefore indicates that the Ni–TiO_2 sample exhibits changes in the low-wavenumber region and additional vibrational features in the N–H/O–H and NH_2 bending regions relative to pure TiO_2. The correspondence between selected absorptions of the parent complex and the modified nanoparticles is consistent with the incorporation of an aniline-containing nickel species at the TiO_2 surface. However, the absence or reduced intensity of some characteristic aniline bands in the modified sample may be related to the relatively low concentration of the nickel-containing component, spectral overlap, or changes in its local environment. Consequently, FTIR alone cannot conclusively establish the coordination geometry, bonding mechanism, or complete retention of the parent complex structure on TiO_2. These observations should therefore be interpreted alongside the XPS, XRD, and Raman results to obtain a more comprehensive understanding of the structural and chemical characteristics of the modified material.

Furthermore, the retention of the characteristic anatase Raman modes, together with their reduced intensities and the absence of substantial peak shifts, suggests that Ni(II)–aniline modification predominantly influences the surface or local interfacial environment of TiO_2 while largely preserving its crystalline framework. This observation is relevant to the subsequent electrocatalytic evaluation, as the enhanced HER/OER performance of Ni–TiO_2 may be associated with surface modification and interfacial effects rather than a major transformation of the TiO_2 crystalline phase. Accordingly, the Raman results complement the XRD and XPS findings by supporting the preservation of the anatase structure and the presence of surface chemical modifications in the Ni–TiO_2 hybrid electrocatalyst.

2.4. X-Ray Photoelectron Spectroscopic Analysis

X-ray photoelectron spectroscopy (XPS) was employed to investigate the surface elemental composition and chemical states of the Ni–TiO_2 NPs. The corresponding survey and high-resolution spectra are presented in Figure 4a–d. The survey spectrum (Figure 4a) displays the characteristic Ti 2p, O 1s, Ni 2p, and C 1s signals, together with the O KLL and Ni LMM Auger features, supporting the presence of Ti-, O-, and Ni-containing species at the sample surface. The Ti and O signals are associated with the TiO_2 framework, whereas the Ni 2p signal confirms the presence of nickel-containing species. The C 1s signal may originate from carbon-containing surface residues, including adventitious carbon and/or residual organic species. The absence of clearly resolved additional crystalline nickel-containing phases in the XRD and Raman analyses, together with the surface-sensitive XPS results, is consistent with nickel species being present in a highly dispersed or poorly crystalline form. However, XPS alone cannot establish whether these species are incorporated into the TiO_2 lattice or associated with its surface.

The high-resolution Ti 2p spectrum (Figure 4b) exhibits two principal components at 458.34 and 464.12 eV, assigned to Ti $2p_{3/2}$ and Ti $2p_{1/2}$, respectively. These binding energies are characteristic of Ti^{4+} in TiO_2. The energy separation of approximately 5.78 eV between the two principal components is consistent with the expected spin–orbit splitting of Ti^{4+}. A higher-binding-energy satellite-related feature is also indicated at 471.66 eV in the fitted spectrum. No distinct lower-binding-energy component attributable to Ti^{3+} is clearly resolved. This observation suggests that titanium predominantly retains its Ti^{4+} oxidation state following modification with the nickel-containing component, without clear XPS evidence of substantial Ti^{4+} reduction [39,40].

The O 1s spectrum (Figure 4c) was resolved into three components at 529.94, 531.61, and 533.02 eV, designated as O(I), O(II), and O(III), respectively. The component at 529.94 eV (O(I)) accounts for 23.96% of the total O 1s signal and is assigned to lattice oxygen associated with Ti–O bonds in TiO_2. The component at 531.61 eV (O(II)), contributing 40.27%, is attributed to surface hydroxyl groups and/or chemically perturbed oxygen at defect or under-coordinated surface sites. Although oxygen vacancies may influence the local oxygen chemical environment, assigning this component exclusively to oxygen vacancies would be premature because surface hydroxyls and other adsorbed oxygen-containing species can contribute within the same binding-energy region. The higher-binding-energy component at 533.02 eV (O(III)), representing 35.77% of the total O 1s signal, is consistent with weakly bound surface oxygen-containing species, such as adsorbed water or oxygenated surface residues [41,42]. The substantial contributions from O(II) and O(III) indicate that surface-associated oxygen species constitute an important fraction of the measured O 1s signal, alongside lattice oxygen. These surface chemical environments may influence interfacial interactions during subsequent electrocatalytic measurements.

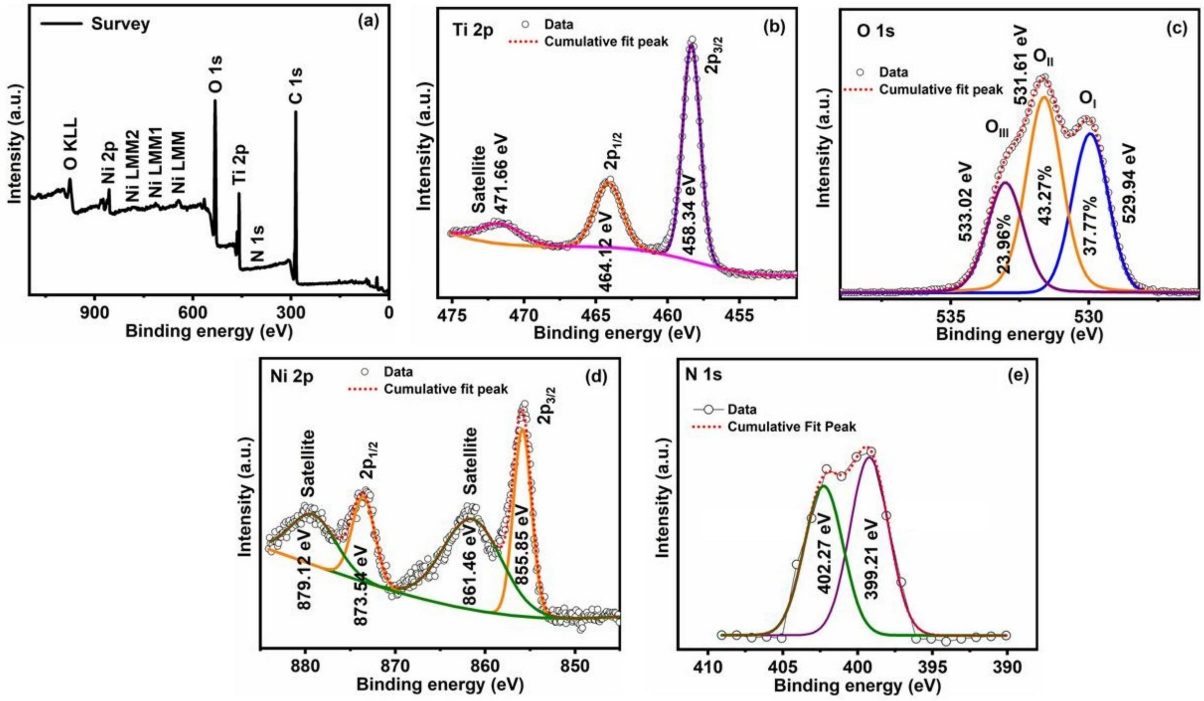


Figure 4. X-ray photoelectron spectroscopy (XPS) investigation of Ni–TiO_2 NPs. (**a**) Survey spectrum showing Ti, O, Ni, and C elements. High-resolution spectra of (**b**) Ti 2p, (**c**) O 1s, (**d**) Ni 2p, and (**e**) N 1s.

The high-resolution Ni 2p spectrum (Figure 4d) provides further evidence for nickel-containing species at the sample surface. The principal peaks are located at 855.85 and 873.54 eV and are assigned to Ni $2p_3/_2$ and Ni $2p_1/_2$, respectively. Additional features at 861.46 and 879.12 eV are attributed to the corresponding shake-up satellite structures. The separation between the two principal Ni 2p components is approximately 17.69 eV, consistent with the characteristic spectral features of Ni^{2+}-containing compounds. The peak positions and accompanying satellite structures support the assignment of the surface nickel species predominantly to an oxidized Ni^{2+} chemical environment. Furthermore, no distinct metallic Ni^0 component is resolved in the lower-binding-energy region typically associated with Ni metal. These observations are chemically consistent with the use of a Ni(II)-containing precursor, although the precise local coordination environment of nickel cannot be established from the Ni 2p spectrum alone.

The high-resolution N 1s spectrum of Ni-modified TiO_2 nanoparticles exhibited two components centred at 399.21 and 402.27 eV (Figure 4e), confirming the presence of nitrogen-containing surface species. The component at 399.21 eV is consistent with amine-type nitrogen originating from the aniline ligands of the $[Ni(aniline)_4Cl_2]$ precursor complex. The additional component at 402.27 eV suggests a second, higher-binding-energy nitrogen environment, potentially associated with protonated or chemically modified nitrogen species. These observations support the retention of aniline-derived nitrogen-containing species on the TiO_2 surface following modification with the nickel–aniline complex.

Overall, the XPS results confirm the presence of Ti, O, Ni, and C on the surface of Ni–TiO_2 NPs, with a weak nitrogen signal resolved in the high-resolution N 1s spectrum (Figure 4e). The Ti 2p spectrum indicates Ti^{4+} predominantly, while the O 1s spectrum reveals contributions from lattice oxygen and surface hydroxyl/chemically perturbed oxygen species. The Ni 2p spectrum supports a predominantly Ni^{2+} chemical environment. The N 1s spectrum exhibits two components at 399.21 and 402.27 eV, assigned to amine-type nitrogen associated with aniline-derived species and a positively charged or chemically modified nitrogen environment, respectively. These findings suggest the partial retention of aniline-derived nitrogen-containing species following surface modification. However, they do not establish the presence of the intact $[Ni(aniline)_4Cl_2]$ complex or a specific Ni–N bonding configuration. Considering the FTIR results, partial ligand dissociation or removal during solution processing and washing, accompanied by the retention of nickel-containing species at oxygenated TiO_2 surface sites, is a plausible interpretation. Thus, the modified surface may comprise nickel-associated oxygen species, residual aniline-derived groups, surface hydroxyls, and adventitious carbon. The absence of additional crystalline nickel-containing phases in the XRD and Raman analyses further supports surface modification while preserving the anatase TiO_2 framework.

The identified surface species, particularly Ni^{2+} and oxygen-containing groups, may influence the interfacial processes involved in HER and OER. Nevertheless, the XPS analysis represents the as-prepared Ni–TiO_2 NPs before electrocatalytic testing; therefore, possible changes in surface composition and chemical states under HER/OER operating conditions cannot be established from the present measurements [43,44].

2.5. Optical and Photoluminescence Properties

The optical and excited-state emission characteristics of pristine TiO_2 and Ni–TiO_2 NPs were examined by steady-state photoluminescence (PL) and time-resolved photoluminescence (TRPL) spectroscopy. The analogous spectra are presented in Figure 5a–d. PL spectroscopy is sensitive to the electronic structure, surface states, defect levels, and radiative recombination pathways of semiconductor materials. In TiO_2, the emission profile can contain aids from near-band-edge/excitonic transitions in addition to radiative recombination over surface and defect-associated states. Subsequently, differences in PL intensity and lifetime offer valuable complementary information concerning the electronic environment and excited-state dynamics of modified TiO_2 materials [45–47].

The PL spectrum recorded at an excitation wavelength of 348 nm (Figure 5a) displays several emission bands for both TiO_2 and Ni–TiO_2, centered at roughly 402.8, 447.9, 465.9, 480.2, 490.5, 566.8, and 614.8 nm. The emission in the near-UV region, mainly around 402.8 nm, can be associated with near-band-edge/excitonic radiative transitions of TiO_2, while the broader emissions spreading throughout the visible region are generally related to localized surface states, structural imperfections, and defect-related energy levels within the TiO_2 band gap [45,46]. Recent studies have likewise reported multiple UV and visible emission components in TiO_2 nanoparticles, with shorter-wavelength emissions related mostly to near-band-edge or excitonic processes and longer-wavelength emissions associated

with surface and defect states. The occurrence of multiple emission components in the present samples then indicates a distribution of radiative electronic states associated with the anatase TiO_2 nanoparticles.

A second PL spectrum measured using an excitation wavelength of 495 nm (Figure 5b) shows emission bands at around 536.5, 552.5, 609.8, 673.5, and 811.7 nm. The presence of these relatively long-wavelength emissions suggests radiative transitions involving localized surface states and sub-band-gap defect-related states rather than direct band-edge recombination alone. Visible and red/near-infrared emissions of TiO_2 have commonly been associated with defect-mediated electronic transitions involving surface states, oxygen-deficiency-related states, and other localized trapping centers [46,48]. A recent analysis of TiO_2 optical properties similarly established that visible emission bands can arise from surface defects and oxygen-deficient environments, highlighting the sensitivity of PL spectra to the surface chemical structure of TiO_2.

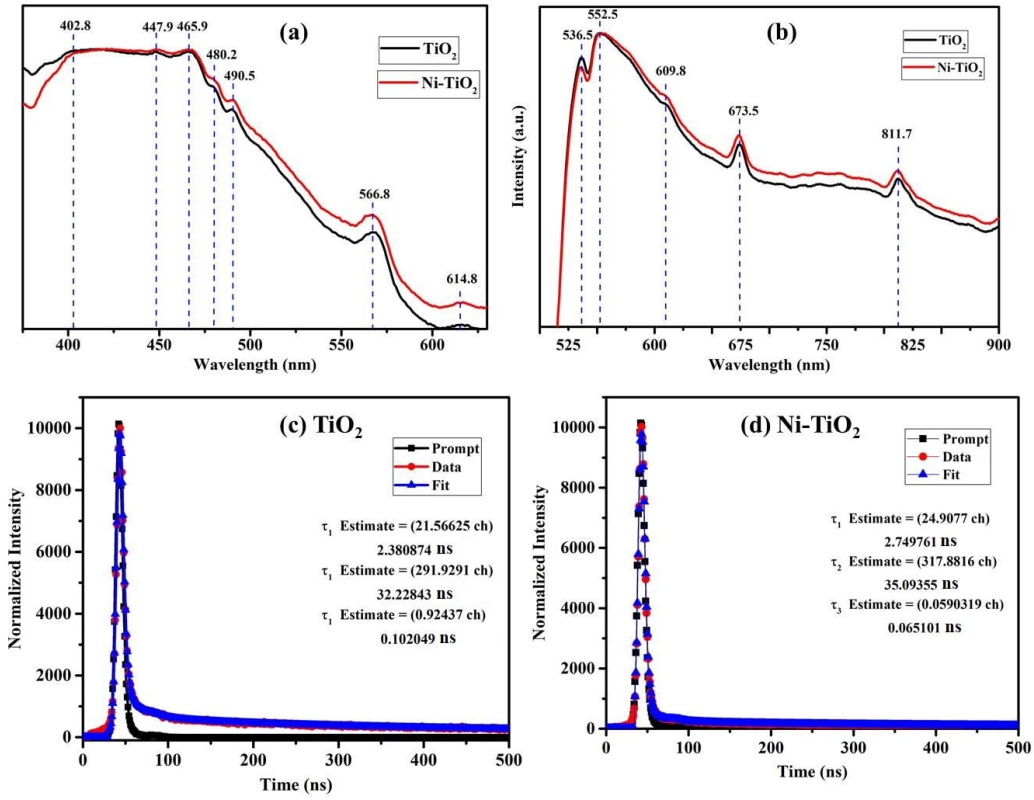


Figure 5. Photoluminescence and time-resolved photoluminescence (TRPL) spectra of pristine TiO_2 and Ni–TiO_2 NPs. (**a**) PL spectra recorded at an excitation wavelength of 348 nm. (**b**) PL spectra recorded at an excitation wavelength of 495 nm. (**c**) TRPL decay profile of pristine TiO_2. (**d**) TRPL decay profile of Ni–TiO_2, with corresponding multi-exponential lifetime components.

Evaluation of the PL spectra shows that the majority of the emission bands of Ni–TiO_2 display a slight increase in intensity relative to pristine TiO_2, while the emission around 536.5 nm shows a small decrease. The absence of a distinct shift in the emission maxima indicates that Ni(II)–aniline modification does not considerably alter the principal radiative transition energies of TiO_2. This observation is consistent with the XRD and Raman results, which demonstrated preservation of the anatase TiO_2 structure without significant changes in the characteristic lattice-related signals. Instead, the difference in emission intensity suggests that Ni(II)–aniline modification mainly influences the population and/or radiative behavior of localized electronic states at the TiO_2 surface. Similar sensitivity of TiO_2 PL intensity to chemical alteration has been reported recently, while the direction

and magnitude of the change depend strongly on dopant concentration, defect density, interfacial structure, and preparation conditions. For instance, Ni modification of TiO_2 nanofibers has been reported to decrease PL intensity at higher Ni contents, demonstrating that the effect of Ni on radiative recombination is not collective and depends on the specific structural and chemical environment of the nickel species [49].

The minor PL enhancement detected for Ni–TiO_2 should therefore be interpreted cautiously. A growth in steady-state PL intensity can show a greater contribution from radiative recombination pathways or an altered population of emitting surface states, rather than necessarily representing enhanced charge separation. Conversely, PL quenching is often understood as suppression of radiative electron–hole recombination, but such clarification also requires supporting evidence because PL intensity is affected by defect concentration, absorption, surface chemistry, excitation efficiency, and other factors [45–47]. In the present Ni–TiO_2 material, the slight increase in most emission bands together with the variations observed in TRPL lifetime thus offers evidence of a modified excited-state environment rather than clear proof of suppressed electron–hole recombination.

More direct evidence concerning the excited-state dynamics was obtained from the TRPL measurements. The decay profile of pristine TiO_2 (Figure 5c) was fitted by three characteristic lifetime components of $\tau_1 = 2.38087$ ns, $\tau_2 = 32.22843$ ns, and $\tau_3 = 0.102049$ ns, while Ni–TiO_2 (Figure 5d) displayed resultant lifetime components of $\tau_1 = 2.749761$ ns, $\tau_2 = 35.09355$ ns, and $\tau_3 = 0.065101$ ns. The first two lifetime components thus increase from 2.38 to 2.75 ns and from 32.23 to 35.09 ns, respectively, after Ni(II)–aniline modification, whereas the shortest component decreases from 0.102 to 0.065 ns. Such multicomponent decay behaviour is characteristic of a heterogeneous semiconductor surface containing more than one recombination or trapping pathway. The fast component can be related to rapid carrier relaxation/recombination pathways, while longer components generally reflect reasonably slower trapping, detrapping, or recombination processes concerning localized states.

The increase in the two longer lifetime components resulting from Ni–TiO_2 formation suggests that a portion of photoexcited carriers experiences slower decay pathways and/or longer-lived trapped states in the modified material. This behaviour indicates that the Ni(II)–aniline environment varies the excited-state dynamics of TiO_2 and introduces or modifies interfacial trapping pathways. In contrast, the shortening of the fastest component suggests that rapid recombination pathways are also modified. Such concurrent changes in fast and slow components are sensible for a heterogeneous surface-modified semiconductor, in which multiple carrier-transfer and trapping processes coexist. Recent studies of modified TiO_2 systems highlight that dopants and interfacial modifiers can alter carrier trapping, defect populations, and charge-transfer dynamics without necessarily creating a shift in the fundamental crystalline phase [45,49].

The increase in the longer-lived components is predominantly notable in the framework of the present electrocatalytic study. While PL/TRPL measurements are achieved under optical excitation and hence do not directly reproduce the charge-transfer processes occurring during HER and OER, the detected lifetime modification proves that the Ni(II)–aniline component perturbs the electronic environment of TiO_2. Such alteration can be attributed to interfacial electronic interaction between Ni-containing species and TiO_2, which may influence carrier localization and surface charge distribution. However, the electrochemical charge-transfer properties related to HER/OER should be recognized mainly from electrochemical parameters such as double-layer capacitance, polarization behaviour, Tafel analysis, and electrochemical impedance rather than inferred merely from PL measurements.

Overall, the PL and TRPL results validate that Ni(II)–aniline alteration varies the optical emission characteristics and excited-state decay dynamics of TiO_2 without con-

siderably shifting the primary emission positions. The minor improvement of most PL bands designates improved radiative pathways, whereas the increase in the longer lifetime components from 2.38 to 2.75 ns and 32.23 to 35.09 ns shows the formation or strengthening of relatively longer-lived electronic states. In conjunction with the XRD and Raman results, these remarks support the view that Ni(II)–aniline alteration primarily changes the surface/interfacial electronic environment of anatase TiO_2 while preserving its underlying crystal structure. These variations afford a vital physicochemical basis for successively examining the impact of Ni–TiO_2 on electrochemical HER and OER activity.

2.6. Electrocatalytic HER Performance

The hydrogen evolution reaction (HER) performance of pristine TiO_2 and the Ni−TiO_2 electrocatalyst was investigated in 1 M KOH using a standard three-electrode configuration at a scan rate of 2 mV s^{-1}. As illustrated in Figure 6a,b, the Ni−TiO_2 exhibits substantially improved HER activity compared with pristine TiO_2. The Ni−TiO_2 catalyst requires overpotentials of 267.2 and 373.1 mV to achieve current densities of 10 and 50 mA cm^{-2}, respectively, whereas pristine TiO_2 requires considerably higher overpotentials of 317.3 and 462.2 mV under the same conditions. Although the HER activity of the Ni−TiO_2 catalyst still requires a higher overpotential than the commercial Pt/C catalyst (110.2 mV at 10 mA cm^{-2}), its markedly improved activity over pristine TiO_2 demonstrates the effectiveness of the Ni(II)-aniline complex modification. Additionally, the contribution of bare Ni foam to the overall HER activity was negligible compared with that of the catalyst-coated samples, indicating that the enhanced hydrogen evolution performance primarily originated from the deposited electrocatalyst. The enhanced HER performance can be attributed to the formation of a well-coupled Ni−TiO_2 heterointerface. The reconstructed Ni species provide catalytic active sites for hydrogen evolution, while the TiO_2 framework offers excellent structural integrity and chemical stability under alkaline conditions. Moreover, the formation of Ni−O−Ti interfacial bonds promotes strong electronic coupling between the two components, facilitating charge transfer across the heterointerface [50,51]. The synergistic interaction between the reconstructed Ni active centers and the TiO_2 support accelerates the overall HER process.

The improved reaction kinetics are further supported by the Tafel analysis shown in Figure 6c. The Ni−TiO_2 catalyst exhibits a Tafel slope of 126.5 mV dec^{-1}, which is lower than that of pristine TiO_2 (163.7 mV dec^{-1}) but higher than that of commercial Pt/C (89.6 mV dec^{-1}). The reduced Tafel slope of Ni−TiO_2 indicates faster HER kinetics compared with pristine TiO_2 and suggests that the reconstructed heterointerface facilitates more efficient proton adsorption and electron transfer during hydrogen evolution. The relatively large Tafel slopes observed for both TiO_2-based catalysts imply that the HER is primarily governed by the Volmer step in alkaline media, where water dissociation is the rate-determining process.

Electrochemical impedance spectroscopy (EIS) further confirms the improved interfacial charge-transfer characteristics (Figure 6d). The Nyquist plot of Ni−TiO_2 exhibits a significantly smaller semicircle than that of pristine TiO_2, indicating a lower charge-transfer resistance (R_{ct}). The reduced Rct demonstrates that the reconstructed Ni−O−Ti interface provides a more efficient electron-conduction pathway, thereby facilitating rapid charge transfer across the electrode/electrolyte interface and improving the HER kinetics.

Figure 6e depicts the N_A present in the electrocatalysts, and the double-layer capacitance was estimated from electrochemical measurements. The calculated number of accessible active sites increased markedly from 0.233×10^{16} for TiO_2 to 18.11×10^{16} for Ni–TiO_2, indicating that the Ni–TiO_2 substantially increases the number of electrochemically available catalytic sites.

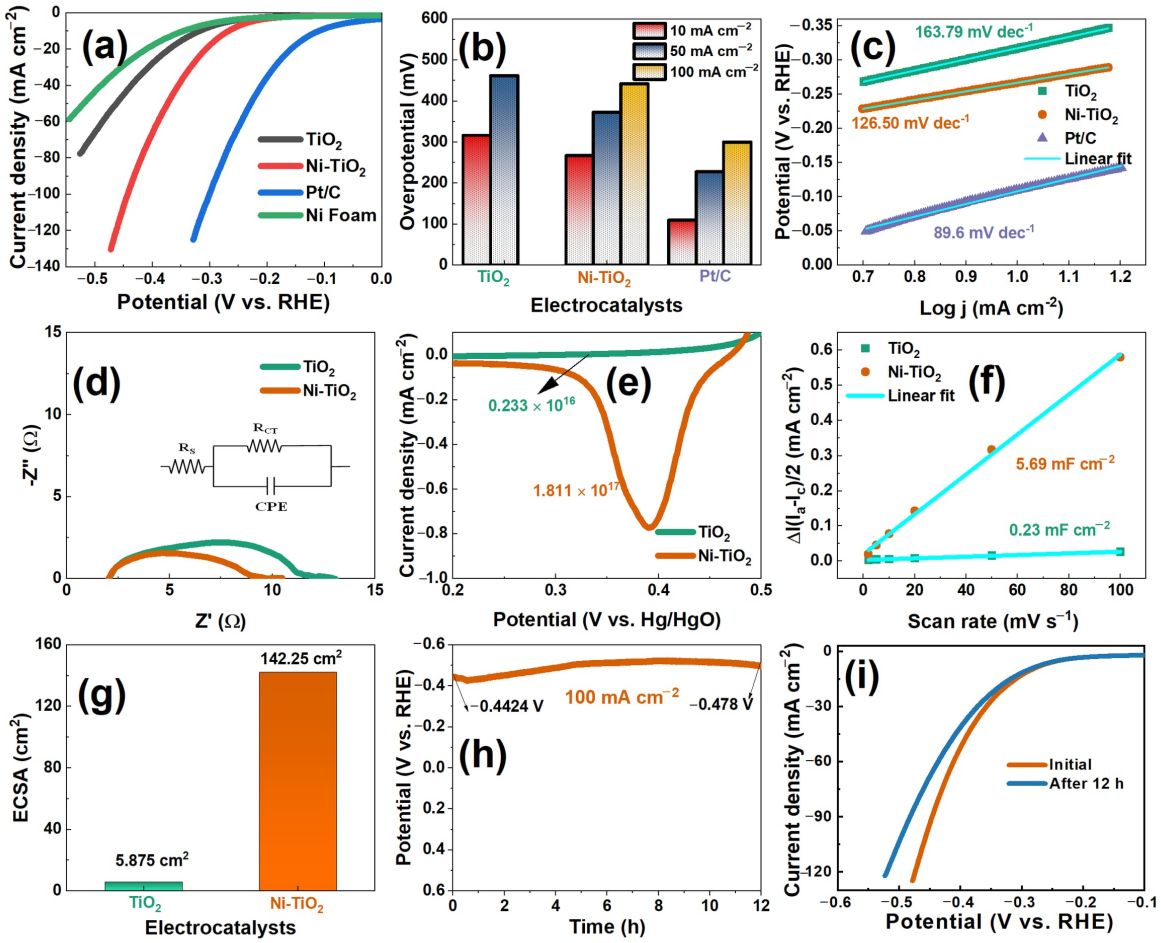


Figure 6. Electrochemical HER performance of TiO_2 and Ni–TiO_2 electrocatalysts in 1 M KOH. (**a**) Polarization curves. (**b**) η at 10, 50, and 100 mA cm^{-2}. (**c**) Tafel plots. (**d**) EIS Nyquist plots. (**e**) Number of active sites (N_A). (**f**) C_{dl}. (**g**) ECSA. (**h**) Chronopotentiometry test. (**i**) Polarization curves before and after 12 h stability test at 100 mA cm^{-2}.

To estimate the density of accessible catalytic active sites, the electrochemical double-layer capacitance (C_{dl}) (Figure 6f) was determined from cyclic voltammetry performed at different scan rates (Figure 7a,b). The calculated C_{dl} value of Ni−TiO_2 (5.69 mF cm^{-2}) is considerably higher than that of pristine TiO_2 (0.23 mF cm^{-2}), corresponding to an electrochemical surface area (ECSA) of 142.25 cm^2 and 5.87 cm^2, respectively (Figure 6g). The increase in ECSA indicates that the Ni–TiO_2 provides a substantially larger number of electrochemically accessible active sites (TiO_2: 0.233 × 10^{16}; Ni–TiO_2: 1.811 × 10^{17}), thereby providing more catalytic centers.

The improved electrochemical properties can be associated with the electronic interaction between Ni species and the TiO_2 support. The incorporation of Ni is expected to modify the local electronic structure of TiO_2, enhancing electrical conductivity and promoting electron mobility across the heterointerface. Such electronic modulation facilitates the transfer of electrons to adsorbed reaction intermediates during HER, thereby reducing the activation energy for hydrogen evolution.

The long-term electrochemical stability of the catalyst was evaluated by chronopotentiometry at a constant current density of 100 mA cm^{-2} for 12 h (Figure 6h). As presented in Figure 6h, the Ni–TiO_2 catalyst maintains stable operation, with a minor increase in overpotential after the chronopotentiometry test. In addition, the polarization curves in Figure 6i exhibit only a small deviation after 12 h of continuous stability testing, confirming

the excellent operational stability of the catalyst. These characteristics highlight the effectiveness of the surface reconstruction strategy for developing stable, low-cost TiO_2-based HER electrocatalysts.

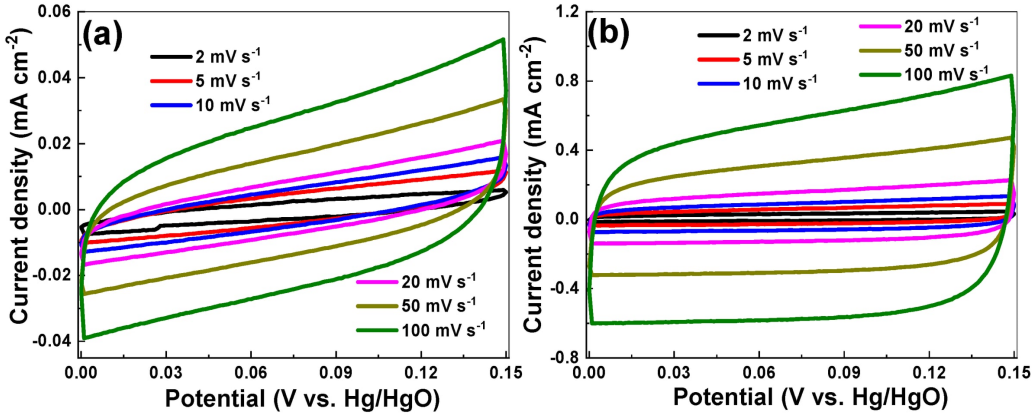


Figure 7. CV profiles from non-Faradaic regions of (**a**) TiO_2 and (**b**) Ni–TiO_2.

These results demonstrate that the Ni(II)-aniline complex modification on the surface of TiO_2 is an effective strategy for enhancing the bifunctional electrocatalytic performance of TiO_2 towards overall water splitting. While the catalyst does not yet match the activity of noble-metal benchmarks, it delivers a compelling combination of improved catalytic activity, excellent stability, and a simple, low-cost synthesis route. Further efforts should focus on tailoring the electronic structure of the Ni–O–Ti heterointerface, identifying the true catalytic activity, and elucidating the reaction mechanism to further improve its overall water-splitting performance.

2.7. Electrocatalytic OER Performance

To evaluate the bifunctional electrocatalytic activity of the synthesized materials, the OER performance of the as-prepared pristine TiO_2 and Ni(II)-aniline complex modification of TiO_2 electrocatalysts was evaluated in 1 M KOH using LSV at a scan rate of 2 mV s^{-1}. As shown in Figure 8a,b, the Ni−TiO_2 catalyst exhibits significantly enhanced OER activity compared with pristine TiO_2 and bare Ni foam at higher current densities. Particularly, the Ni−TiO_2 electrocatalyst requires an overpotential of 381.3 mV to achieve a current density of 50 mA cm^{-2}, whereas pristine TiO_2 requires a substantially higher overpotential of 500.5 mV to reach the same current density. Notably, the overpotential of the Ni−TiO_2 catalyst approaches the commercial RuO_2 benchmark under identical experimental conditions (298.2 mV for 50 mA cm^{-2}), demonstrating the effectiveness of the Ni(II)-aniline complex modification in enhancing the OER catalytic activity of TiO_2. In addition, the bare Ni foam sample exhibited substantially lower OER activity than the catalyst-loaded electrodes, highlighting the dominant role of the deposited electrocatalyst in enhancing the OER behavior.

The improved reaction kinetics are further confirmed by Tafel analysis (Figure 8c). The Ni−TiO_2 electrode exhibits a Tafel slope of 86.7 mV dec^{-1}, which is considerably lower than that of pristine TiO_2 (143.4 mV dec^{-1}) and slightly higher than commercial RuO_2 (58.1 mV dec^{-1}). The reduced Tafel slope indicates accelerated reaction kinetics and more efficient charge-transfer processes during oxygen evolution. This improvement suggests that the reconstructed Ni−TiO_2 interface effectively lowers the kinetic barrier for the formation of oxygen-containing intermediates, thereby facilitating faster OER kinetics.

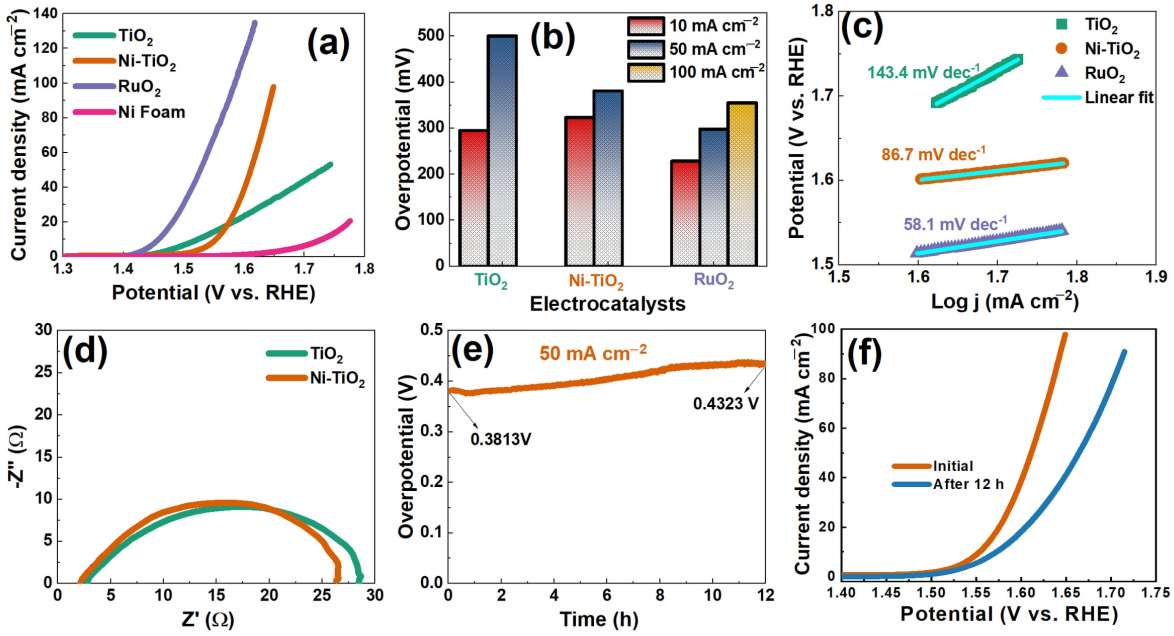


Figure 8. Electrochemical OER performance and stability of TiO_2 and Ni–TiO_2 electrocatalysts. (**a**) Polarization curves. (**b**) η at 10, 50, and 100 mA cm^{-2}. (**c**) Tafel plots. (**d**) EIS Nyquist plots. (**e**) Chronopotentiometry test. (**f**) Polarization curves before and after 12 h stability test at 50 mA cm^{-2}.

Electrochemical impedance spectroscopy (EIS) further supports the enhanced catalytic performance (Figure 8d). The Nyquist plot of Ni–TiO_2 displays a noticeably smaller semicircle than that of pristine TiO_2, indicating a lower charge-transfer resistance (R_{ct}). The reduced interfacial resistance facilitates faster electron transport between the electrode surface and electrolyte, thereby improving the overall OER kinetics.

The Ni–TiO_2 catalyst achieves an overpotential of 381.3 mV at 50 mA cm^{-2}. During the 12 h chronopotentiometry stability test at a constant current density of 50 mA cm^{-2}, the electrode potential increased from 0.3813 to 0.4323 V, retaining 88.2% of its initial performance. This relatively small overpotential variation indicates good operational stability under continuous OER conditions (Figure 8e). The polarization curves in Figure 8f show only a very slight decrease after 12 h of continuous stability testing. Although several reported catalysts exhibit lower overpotentials or smaller Tafel slopes, the present catalyst provides a favorable balance between catalytic activity, durability, and the simplicity of the synthesis route. These characteristics demonstrate the potential of Ni(II)-aniline complex modification for developing efficient and stable TiO_2-based OER electrocatalysts.

The structural and morphological analysis of the Ni–TiO_2 electrocatalyst after the OER stability test was investigated using XRD, FE-SEM, and EDX analyses, as shown in Figure 9. The post-OER XRD pattern (Figure 9a) was examined to evaluate the structural characteristics of the catalyst after prolonged electrochemical operation. As shown in Figure 9a, the post-OER XRD spectra showed no obvious change, confirming its relative structural stability. The FE-SEM image (Figure 9b) reveals an aggregated morphology, which may be attributed to surface reconstruction during electrochemical operation, potentially accompanied by the formation of oxyhydroxide species under OER conditions. Furthermore, the EDAX spectrum (Figure 9c) confirms the presence of Ti, O, and Ni in the post-OER electrode. This result further supports the formation of an oxyhydroxide surface layer during prolonged OER electrolysis.

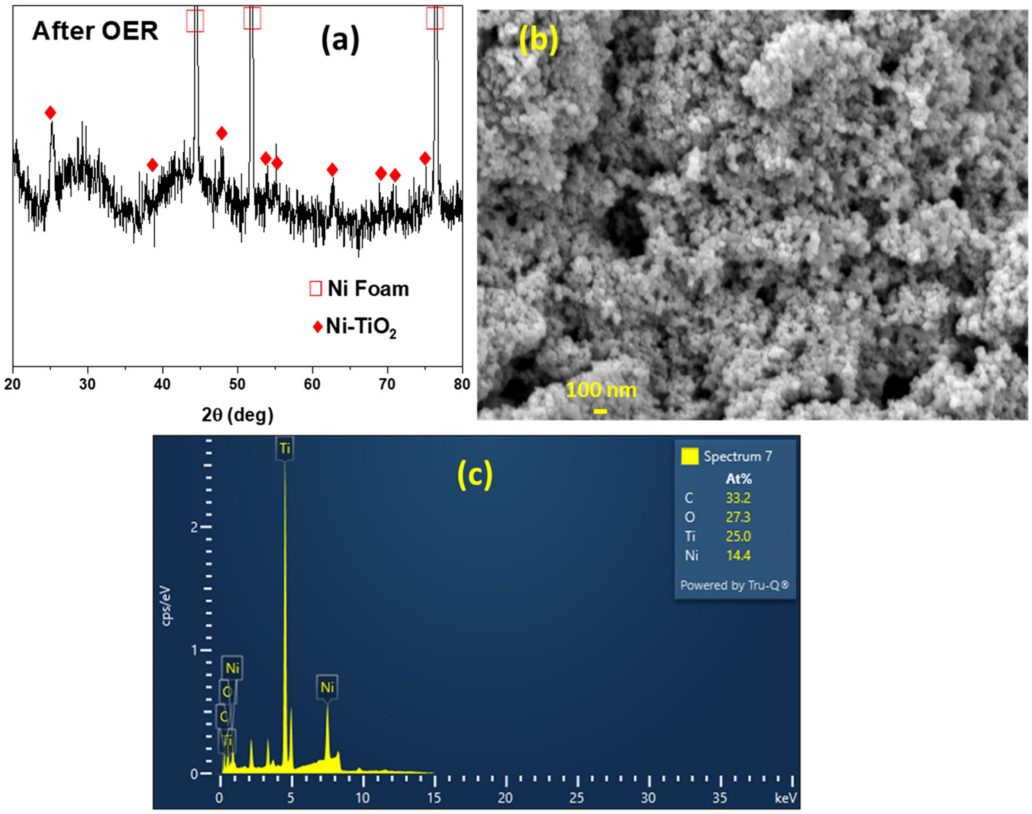


Figure 9. Post-OER performance of Ni–TiO_2 electrocatalyst: (**a**) XRD; (**b**) FE-SEM; (**c**) EDAX.

3. Materials and Methods

3.1. Materials and Characterization Methods

Nanocrystalline anatase TiO_2 nanoparticles (surface area: 200–220 m^2 g^{-1}; average particle size: approximately 25 nm) were used as the inorganic host nanomaterial. The previously synthesized dichloridotetrakis(benzenamine)nickel(II) (aniline complex of nickel(II)), $[Ni(C_6H_5NH_2)_4Cl_2]$ or $[Ni(aniline)_4Cl_2]$, was used as the nickel-containing precursor for surface modification of TiO_2. The Ni(II)–aniline complex was produced and recrystallized according to a previously reported procedure [25]. Aniline (An) served as the coordinating ligand in the precursor complex. All other chemicals and reagents were of analytical grade and used as received without further purification. Distilled/deionized water was used throughout the synthesis and experimental procedures.

The crystalline phases of the prepared materials were examined by powder X-ray diffraction (PXRD) using a Philips/PANalytical (Almelo, The Netherlands) diffractometer equipped with Cu Kα radiation. Surface morphology and elemental composition were characterized using field-emission scanning electron microscopy (FE-SEM) coupled with energy-dispersive X-ray (EDX) spectroscopy (JEOL IT800, Tokyo, Japan). Fourier-transform infrared (FTIR) spectra were documented in the range of 400–2000 cm^{-1} using a Thermo Nicolet 6700 FTIR spectrophotometer (Madison, WI, USA) with KBr pellets. Raman spectra were obtained using a Renishaw inVia Raman microscope equipped with appropriate laser excitation. The optical properties were inspected by diffuse reflectance UV–visible spectroscopy (DRS) in the wavelength range of 200–800 nm using a Shimadzu UV-2450 PC spectrophotometer (Tokyo, Japan), with $BaSO_4$ used as the reference material.

Steady-state photoluminescence (PL) spectra were recorded using a Horiba–Jobin Yvon SPEX-SF13-11 (Kyoto, Japan) spectrofluorophotometer equipped with a xenon lamp. PL measurements were performed using excitation wavelengths of 348 and 495 nm, as

suitable for the respective emission measurements. Time-resolved photoluminescence (TRPL) measurements were carried out to estimate the excited-state decay characteristics of the samples.

The surface elemental composition and chemical states of the Ni–TiO_2 nanoparticles (NPs) were studied by X-ray photoelectron spectroscopy (XPS) using a SPECS SAGE 100 spectrometer equipped with a Mg Kα X-ray source, which operated at 20 mA and 12.5 kV. The XPS spectra were used to identify the Ti, O, Ni, and C surface components and to determine their corresponding chemical environments.

3.2. Surface Modification of Anatase TiO_2 Nanoparticles with the Ni(II)–Aniline Complex

The Ni(II)–aniline-modified TiO_2 nanoparticles (Ni–TiO_2 NPs) were prepared using a simple aqueous surface-modification procedure. First, 0.10 g of [Ni(aniline)$_4$Cl$_2$] complex (1.65 mM) was dissolved in distilled water in a 125 mL stoppered bottle. Then, 200 mg of anatase TiO_2 nanoparticles were added to the precursor solution.

The resulting suspension was placed in a temperature-controlled Technico cooling water-bath shaker and constantly agitated for 240 min at 298 K to assist interaction between the Ni(II)–aniline complex and the TiO_2 nanoparticle surface. Following the reaction period, the solid product was separated from the suspension by centrifugation. The improved material was frequently washed with distilled water to remove weakly adsorbed and residual soluble species. The purified solid was consequently dried at room temperature to obtain the Ni(II)–aniline complex-modified TiO_2 nanoparticles (Ni–TiO_2 NPs).

The prepared Ni–TiO_2 material was then exposed to structural, vibrational, optical, morphological, and surface-chemical characterization using PXRD, FTIR, Raman, DRS, PL, TRPL, and XPS. Pristine TiO_2 NPs prepared under identical handling conditions were used as the reference material for comparison [26,27].

3.3. Electrocatalytic Analysis of HER and OER

The electrocatalytic measurements were performed using a three-electrode configuration comprising Hg/HgO as the reference electrode and Pt foil as the counter electrode, coupled to a CHI660F electrochemical workstation. The catalysts were coated onto the NF substrate at approximately 2 mg, with supporting carbon black and PVDF, respectively. For comparison, 2 mg of commercial Pt/C and RuO_2 catalysts were also coated on the NF substrate and analysed. The coated samples were dried at 60 °C. Linear sweep voltammetry (LSV) measurements for both HER and OER were conducted in 1 M KOH electrolyte at a scan rate of 2 mV s^{-1}. Electrochemical impedance spectroscopy (EIS) measurements were performed over a frequency range of 0.01 Hz to 100 kHz using an amplitude of 10 mV [28].

All the measured potentials were converted to the reversible hydrogen electrode (RHE) scale according to Equation (1). The overpotential (η) and Tafel slope were determined using Equations (2) and (3), respectively.

$$E_{RHE} = E_{Hg/HgO} + 0.059\,pH + 0.098 \quad (1)$$

$$\eta = E_{RHE} - 1.23 \quad (2)$$

$$\eta = b\log j + a \quad (3)$$

The ECSA was determined from the double-layer capacitance (C_{dl}) obtained from cyclic voltammetry (CV) measurements performed within the non-Faradaic region, as given by Equation (4). A specific capacitance of 40 μF cm^{-2} was employed to convert the C_{dl} values into ECSA, assuming a flat electrode surface with a geometric area of 1.0 cm^{-2}.

$$ECSA = (C_{dl}/\ 40\ \mu F\ cm^{-2})cm^2 \quad (4)$$

The charge associated with the reduction peak (Q) was determined using Equation (5):

$$Q = \frac{\int I\, dV}{v} \quad (5)$$

Here, Q(C) represents the total charge corresponding to the reduction peak, and v denotes the scan rate ($mV\ s^{-1}$). Assuming a single-electron transfer process, the number of surface-active sites (N_A) was calculated using Equation (6), where $q = 1.602 \times 10^{-19}$ C.

$$N = \frac{Q}{q} \quad (6)$$

4. Conclusions

In summary, a Ni(II)–aniline complex-modified TiO_2 (Ni–TiO_2) nanomaterial was successfully prepared over a simple aqueous surface-modification itinerary and examined as a bifunctional electrocatalyst for alkaline water splitting. XRD, FTIR, and Raman analyses established that the anatase TiO_2 structure was conserved after modification, with no noticeable additional crystalline nickel-containing phase. The unaffected Raman peak positions, along with reduced band intensities, indicate that the modification primarily affects the local surface environment without appreciably disturbing the TiO_2 crystal structure. XPS analysis further confirmed the presence of Ti, O, Ni, C, and N-containing species at the surface, with Ti predominantly in the Ti^{4+} state, nickel in a predominantly Ni^{2+} chemical environment, and nitrogen consistent with aniline-derived surface species. The optical and time-resolved photoluminescence results established that Ni(II)–aniline modification changed the emission characteristics and excited-state decay behaviour of TiO_2, representing changes in its surface and interfacial electronic environment.

The electrochemical studies established a clear beneficial effect of Ni(II)–aniline modification on the HER performance of TiO_2. Ni–TiO_2 required overpotentials of 267.2 and 373.1 mV to attain current densities of 10 and 50 mA cm^{-2}, respectively, compared with 317.3 and 462.2 mV for pristine TiO_2. The lower HER Tafel slope of Ni–TiO_2 (126.5 mV dec^{-1}) relative to TiO_2 (163.7 mV dec^{-1}) further indicates enhanced reaction kinetics. The considerable increase in double-layer capacitance from 0.23 to 5.69 mF cm^{-2} and ECSA from 5.87 to 142.25 cm^2 indicates a much better electrochemically accessible surface area following Ni(II)–aniline modification. Reliably, the estimated number of accessible active sites increased markedly from 0.233×10^{16} to 1.811 × 1017. The Ni–TiO_2 electrode also presented excellent HER durability, retaining 92.55% of its initial activity after 12 h of continuous operation at 100 mA cm^{-2}.

For OER, Ni–TiO_2 exhibited a clear advantage at higher current density, reaching 50 mA cm^{-2} at an overpotential of 381.3 mV, considerably lower than the 500.5 mV required by pristine TiO_2. The OER Tafel slope reduced from 143.4 mV dec^{-1} for TiO_2 to 86.7 mV dec^{-1} for Ni–TiO_2, representing markedly improved reaction kinetics. While pristine TiO_2 exhibited a lower overpotential at 10 mA cm^{-2}, the higher high-current-density response and greatly reduced Tafel slope of Ni–TiO_2 highlight the beneficial role of Ni(II)–aniline modification under more challenging operating conditions. Moreover, Ni–TiO_2 preserved 88.2% current retention after 12 h of continuous OER operation at 50 mA cm^{-2}, endorsing its good operational stability. Surface characterization of Ni–TiO_2 NPs before and after OER testing revealed changes in their morphological and elemental features following electrocatalytic operation.

Overall, the combined structural, spectroscopic, surface-chemical, and electrochemical results establish that integration of the Ni(II)–aniline complex considerably modifies the surface and electrochemical properties of TiO_2 and improves its HER/OER performance, mainly its high-current-density activity, manageable active-site population, reaction kinetics,

and long-term stability. The current work hence establishes Ni(II)–aniline functionalization as a promising coordination-chemistry-assisted approach for improving the electrocatalytic properties of TiO_2, providing a simple route toward earth-abundant materials for alkaline water-splitting applications.

Author Contributions: J.S., M.N.R., E.S., R.K. and G.A.S.: conceptualization, software, validation, investigation, writing—original draft preparation, writing—review and editing, and visualization; J.W.: supervision; G.A.S. and J.W.: project administration; J.W.: funding acquisition. All authors have read and agreed to the published version of the manuscript.

Funding: This research was funded by the National Natural Science Foundation of China (W2412116, 22350410386, 22375200, U22A20394) and the International Partnership Program of the Chinese Academy of Sciences (028GJHZ2023097GC).

Data Availability Statement: Data will be made available on request.

Acknowledgments: This work was partially carried out using the facilities of UGC-DAE CSR. The authors acknowledge financial support from UGC-DAE CSR through a Collaborative Research Scheme (CRS) (project number: CRS/2023-24/01/1012).

Conflicts of Interest: The authors declare no conflicts of interest.

References

1. Li, J.; Naren, G.; Tang, C.; Xing, L.; Meng, L.; Wang, N.; Zhang, R.; Ye, S.; Wang, L.; Du, L. Asymmetric ruthenium-iron dipole enabling fast alkaline water splitting on ruthenium-doped iron-nickel layered double hydroxides. *Mater. Rep. Energy* **2025**, *5*, 100359. [CrossRef]
2. Zhang, K.; Wu, L.; Xu, X.; Shao, Z.; An, L. Engineering the dynamic reactant–electrode interface in electroreduction systems: Advances, challenges and prospects. *Chem. Soc. Rev.* **2026**, *55*, 9082–9146. [CrossRef]
3. Habib, M.A.; Singh, M.; Kim, H.; Park, J.; Kim, S.; Cha, D.C.; Jung, J.; Yeo, Y.S.; Yoo, S.; Lee, J.; et al. High-entropy materials for electrocatalysis: Fundamentals, design, and applications in OER/ORR. *Int. J. Hydrogen Energy* **2026**, *276*, 157566. [CrossRef]
4. Habib, M.A.; Dristy, S.A.; Lin, S.; Joni, M.H.; Najibullah, M.; Mandavkar, R.; Lee, J. Electrochemical-doping of tungsten on nickel-boron-phosphide microspheres for accelerated industrial-scale water electrolysis at high current density. *Adv. Mater. Technol.* **2025**, *10*, 70021. [CrossRef]
5. Zheng, X.; Zhou, Z.; Wang, J.; Zhao, Z.; Zhou, J. Advanced Electrolytic Water Catalysts: A Key Technology Empowering China's "Dual Carbon" Strategy. *Catalysts* **2026**, *16*, 475. [CrossRef]
6. Nikolić, V.M.; Dimić-Mišić, K.M.; Maslovara, S.L.; Popović, D.P.; Gigov, M.N.; Krstić, S.S.; Marčeta Kaninski, M.P. Advances in Alkaline Water Electrolysis—The Role of In Situ Ionic Activation in Green Hydrogen Production. *Catalysts* **2026**, *16*, 98. [CrossRef]
7. Ashok, R.; Sakthivel, T.G. Waste-derived electrocatalysts for green hydrogen production: Standardized benchmarking, techno-economic translation, and circular engineering barriers. *Environ. Prog. Sustain. Energy* **2026**, e70540. [CrossRef]
8. Wu, X.; Zhang, L.; Gao, Y.; Feng, X.; Bai, Y.; Ma, W.; Zhang, H.; Zhao, B.; Zheng, Y. Alkaline Water Electrolysis Catalysts: Mechanisms, Design Strategies, and Advancements. *ChemNanoMat* **2026**, *12*, e70269. [CrossRef]
9. Perović, I.M.; Mitrović, S.D.; Brković, S.M.; Pašti, I.A. Advances in nickel-based catalysts for alkaline water electrolysis: Comprehensive review of current research direction for HER and OER applications. *Chem. Rec.* **2025**, *25*, e202500049. [CrossRef]
10. Wesley, G.; Swetlech, E.; Velasco, C.; Williams, A.; Larsen, K.; Antony Jose, S.; Menezes, P.L. Catalytic Materials for Hydrogen Generation: Design, Properties, and Applications in Sustainable Energy Systems. *Processes* **2026**, *14*, 957. [CrossRef]
11. Khan, S.; Ashraf, M.; Zahid, T.; El-Sabban, H.A.; El Maati, L.A.; Asadulaeva, S.; Sunny, M.A.; Kumar, A.; Oza, A.D.; Tawfik, S.G.; et al. Improving hydrogen evolution reaction and energy storage efficiency using Ni-MOF/In_2S_3@ g-C_3N_4 materials as advanced functional platform. *J. Mater. Sci. Mater. Electron.* **2026**, *37*, 1549. [CrossRef]
12. San, X.; Wu, W.; Zhang, L.; Meng, D.; Shao, H.; Qi, J. Recent advances in local regulation of nickel-based catalysts for electrocatalytic water splitting. *Int. J. Hydrogen Energy* **2025**, *168*, 151097. [CrossRef]
13. Ma, R.; Tang, Y.; He, Z.; Li, Y.; Wang, X. Advances and enhancement strategies in nickel-based electrocatalysts for oxygen evolution reaction. *ACS Appl. Energy Mater.* **2025**, *8*, 7883–7897. [CrossRef]
14. Lizcano-Vaquero, R.; Burón, R.; Recio, F.J.; Jiménez-Gómez, D.; Calatayud, D.G.; Iglesias-Juez, A.; Fresno, F.; Mendiola, M.A.; López-Torres, E. Nickel (II) benzil bis (Thiosemicarbazonato) complexes as electrocatalysts for hydrogen evolution reaction. *Appl. Organomet. Chem.* **2025**, *39*, e70094. [CrossRef]

15. Wang, C.; Yang, N.; Cai, D.; Zhan, S.Z.; Liu, K. Synthesis, characterization and investigation electrocatalytic property of nickel (II) complex based on 1, 2-bis (diphenylphosphino) ethane for hydrogen generation and hydrogen oxidation. *J. Mol. Struct.* **2025**, *1333*, 141702. [CrossRef]
16. Le, L.H.; Pham, N.H.; Tran, P.D.; To, T.H. Synthesis of an imine-type nickel complex and investigation of its electrocatalytic activity for H2 evolution. *RSC Adv.* **2025**, *15*, 2430–2436. [CrossRef]
17. Baig, K.M.Y.; Marimuthu, S.; Maduraiveeran, G.; Kole, G.K. One-dimensional nickel (ii) coordination polymers of 9-anthracenyl-4′-benzoate and bispyridyl linkers as efficient electrocatalysts for hydrogen and oxygen evolution reactions. *Dalton Trans.* **2025**, *54*, 11025–11035. [CrossRef]
18. Paul, A.; Gusmão, F.; Mahmoud, A.G.; Hazra, S.; Rakočević, L.; Šljukić, B.; Khan, R.A.; Guedes da Silva, M.F.C.; Pombeiro, A.J. Catalyzing towards clean energy: Tuning the oxygen evolution reaction by amide-functionalized Co (ii) and Ni (ii) pristine coordination polymers. *CrystEngComm* **2024**, *26*, 2755–2764. [CrossRef]
19. Song, F.; Li, W.; Han, G.; Sun, Y. Electropolymerization of aniline on nickel-based electrocatalysts substantially enhances their performance for hydrogen evolution. *ACS Appl. Energy Mater.* **2018**, *1*, 3–8. [CrossRef]
20. Rajkumar, T.; Navaneethan, S.; Saravanan, V.; Ramamoorthy, R. Biomass-derived rGO–Ni, co mixed-oxide counter electrodes: A sustainable route to Pt-free DSSCs. *Waste Biomass Valorization* **2026**, *17*, 4621–4636. [CrossRef]
21. Mohamed, S.B.; Baraneedharan, P.; V, K.D.; Jalaludeen, A.M.; Sirajuddeen, M.M.S.; Vinayagam, S.; Selvam, M.K.; Ramakrishnan, P.; Sundaram, T. Titanium Dioxide Nanotubes for Regenerative and Translational Applications: Advances in Synthesis, Functionalization, and Biomedical Integration. *Regen. Eng. Transl. Med.* **2026**, 1–28. [CrossRef]
22. Sead, F.F.; Jain, V.; Roopashree, R.; Devi, A.; Kashyap, A.; Sharma, G.C.; Bhakuni, P.N.; Kazemi, M.; Noorizadeh, H. Engineering TiO_2-based nanostructures for enhanced electrocatalytic and photocatalytic redox reactions. *Results Chem.* **2025**, *17*, 102544. [CrossRef]
23. Qiao, R.; Zhang, K.; Wei, S.; Bai, H.; Zhang, Z.; Li, J.; Liu, G. Titanium dioxide induced nickel-iron alloy-based precatalyst towards efficient and durable oxygen evolution reaction. *J. Alloys Compd.* **2024**, *1004*, 175729. [CrossRef]
24. Li, Z.; Zhang, K.; Wei, S.; Zhang, Z.; Han, H.; Liu, G. Titanium oxide supported molybdenum-nickel-iron oxide electrocatalyst for efficient and durable oxygen evolution reaction. *Fuel* **2024**, *375*, 132509. [CrossRef]
25. Subashini, R.; Sundaram, G.A. Biological Activity of Nickel(II)-R-Aniline Complexes. *Teresian Int. J. Chem. Sci.* **2023**, *IV*, 9–24.
26. Sundaram, G.A.; Murugesan, D.; Kanniah, R.; Muniyandi, G.R.; Ramesh, L.; Alagarsamy, S.K.K. Synthesis, Characterization, Antibacterial and Photocatalytic Studies of Metal Oxides Coupled Nanocomposites. *ChemistrySelect* **2024**, *9*, e202302470. [CrossRef]
27. Ganeshraja, A.S.; Thirumurugan, S.; Rajkumar, K.; Zhu, K.; Wang, Y.; Anbalagan, K.; Wang, J. Effects of structural, optical and ferromagnetic states on the photocatalytic activities of Sn-TiO_2 nanocrystals. *RSC Adv.* **2016**, *6*, 409. [CrossRef]
28. Sundaram, G.A.; Kulandaivelu, K.; Manikandan, V.; Viswanathan, M.R.; Valdés, H.; Anbalagan, K.; Bhatt, C.S.; Wang, J. Photoassisted synthesis of Co–TiO_2 nanoparticles with enhanced bifunctional electro-catalytic activity for HER and OER. *J. Alloys Compd.* **2026**, *1073*, 189044. [CrossRef]
29. Damkale, S.R.; Arbuj, S.S.; Umarji, G.G.; Rane, S.B.; Kale, B.B. Highly crystalline anatase TiO_2 nanocuboids as an efficient photocatalyst for hydrogen generation. *RSC Adv.* **2021**, *11*, 7587–7599. [CrossRef]
30. Nelson, K.; Mecha, A.C.; Kumar, A. Characterization of novel solar based nitrogen doped titanium dioxide photocatalytic membrane for wastewater treatment. *Heliyon* **2024**, *10*, e29806. [CrossRef]
31. Birla, P.N.; Arbuj, S.; Shinde, M.D.; Joseph, S.; Rane, S.; Kulkarni, S.; Kale, B. Electroless Ni plated nanostructured TiO_2 as a photocatalyst for solar hydrogen production. *RSC Adv.* **2023**, *13*, 20068–20080. [CrossRef]
32. Liu, Y.; Luo, Y.; Ye, J.; Zhao, L.; Chen, Y.; Dai, Y.; Xie, Y.; Wang, Y.; Zhang, Y. Photocatalytic hydrogen production performance of anatase and brookite TiO_2 based on oxygen vacancies and noble metal Pt modification. *J. Photochem. Photobiol. A Chem.* **2026**, *479*, 117242. [CrossRef]
33. Alias, N.; Mirzakhani, N.; Hussain, Z.; Tan, W.K.; Kawamura, G.; Matsuda, A.; Lockman, Z. Formation of titanium dioxide nanotubes on Ti–Ni alloys by anodization for Cr (VI) removal from wastewater. *ACS Omega* **2025**, *10*, 47038. [CrossRef]
34. Devi, N.S.; Pachaiappan, R.; Nayak, A.K.; Baig, A.B.A.; Velusamy, S.; Ramachandran, T.; Cornejo-Ponce, L. Synthesis and characterization of Cu decorated WO_3/TiO_2 for photocatalytic and antimicrobial applications. *Chem. Pap.* **2026**, *80*, 8297–8316. [CrossRef]
35. Hazem, R.; Izerrouken, M.; Cheraitia, A.; Djehlane, A. Raman study of ion beam irradiation damage on nanostructured TiO_2 thin film. *Nucl. Instrum. Methods Phys. Res. Sect. B Beam Interact. Mater. At.* **2019**, *444*, 62–67. [CrossRef]
36. Neris, A.M.; Salvador, C.; Silva, U.C.; Chesman, C.; Machado, G.; Longo, E.; Santos, I.M. Magnetic photocatalysts based on ferrite@ZrO_2@TiO_2 core-shell systems for degradation of aqueous pollutants. *Mater. Sci. Eng. B* **2026**, *327*, 119241. [CrossRef]
37. Dhotre, S.B.; Lonkar, S.P.; Bhosale, A.S.; Mali, N.P.; Kaswan, P.; Mene, R.U.; Takale, S.P.; Bhujbal, N.N. Solar-driven degradation of eosin Y using Cu–TiO_2 Photocatalysts: A comparative study of sol–gel and hydrothermal synthesis routes. *Inorg. Chem. Commun.* **2025**, *184*, 115943. [CrossRef]

38. Ganeshraja, A.S.; Thirumurugan, S.; Rajkumar, K.; Wang, J.; Anbalagan, K. Ferromagnetic nickel (II) imidazole-anatase framework: An enhanced photocatalytic performance. *J. Alloys Compd.* **2017**, *706*, 485–494. [CrossRef]
39. Altomare, M.; Qin, S.; Saveleva, V.A.; Badura, Z.; Tomanec, O.; Mazare, A.; Zoppellaro, G.; Vertova, A.; Taglietti, A.; Minguzzi, A.; et al. Metastable Ni(I)-TiO_{2-x} photocatalysts: Self-amplifying H_2 evolution from plain water without noble metal Co-catalyst and sacrificial agent. *J. Am. Chem. Soc.* **2023**, *145*, 26122. [CrossRef]
40. Tian, X.; Ren, R.; Wei, F.; Pei, J.; Zhuang, Z.; Zhuang, L.; Sheng, W. Metal-support interaction boosts the stability of Ni-based electrocatalysts for alkaline hydrogen oxidation. *Nat. Commun.* **2024**, *15*, 76. [CrossRef]
41. Podelinska, A.; Neilande, E.; Pankratova, V.; Serga, V.; Bandarenka, H.; Burko, A.; Piskunov, S.; Pankratov, V.A.; Sarakovskis, A.; Popov, A.I.; et al. Structural and Spectroscopic Characterization of TiO_2 Nanocrystalline Materials Synthesized by Different Methods. *Nanomaterials* **2025**, *15*, 498. [CrossRef]
42. Gao, J.; Alsaab, H.O.; Zare, M.H.; Shirazian, S. Magnesiothermal reduction and doping strategies in engineered TiO_2 for pharmaceutical degradation and CO_2 conversion. *npj Clean Water* **2025**, *8*, 76. [CrossRef]
43. Płacheta, K.; van Spronsen, M.A.; Ferrer, P.; Radecka, M.; Zakrzewska, K. Surface and bulk properties of black, blue and transparent TiOx thin-film photoanodes for green hydrogen generation by water splitting. *J. Mater. Chem. A* **2025**, *13*, 30191–30203. [CrossRef]
44. Yang, G.; Kim, J.; Lee, B.; Jang, J.E.; Kwon, H.J. One-Step Laser-Induced Oxidation and Doping for Tailored p-Type Conversion of Al-Doped TiO_2. *Small* **2025**, *21*, 2502139. [CrossRef]
45. Mulus, D.A.S.; Permana, M.D.; Deawati, Y.; Eddy, D.R. A current review of TiO_2 thin films: Synthesis and modification effect to the mechanism and photocatalytic activity. *Appl. Surf. Sci. Adv.* **2025**, *27*, 100746. [CrossRef]
46. Jadhav, A.J.; Goswami, A.D.; Trivedi, D.H.; Chavan, P.V.; Jadhav, N.L.; Pinjari, D.V. A comprehensive review on pure and doped titanium oxide nanoparticles for photocatalytic applications. *Inorg. Chem. Commun.* **2025**, *181*, 115206. [CrossRef]
47. Liang, X.; Yu, S.; Meng, B.; Wang, X.; Yang, C.; Shi, C.; Ding, J. Advanced TiO_2-based photoelectrocatalysis: Material modifications, charge dynamics, and environmental–energy applications. *Catalysts* **2025**, *15*, 542. [CrossRef]
48. Cremades, A.; Hidalgo, P.; Maestre, D.; Martínez-Casado, R.; Nogales, E.; Rodríguez, B.; Vásquez, G.C.; Méndez, B. Opportunities of semiconducting oxide nanostructures as advanced luminescent materials in photonics. *Adv. Mater.* **2025**, *38*, e12456. [CrossRef]
49. Ahmetović, S.; Vasiljević, Z.Ž.; Krstić, J.B.; Finšgar, M.; Solonenko, D.; Bartolić, D.; Tadić, N.B.; Miskovic, G.; Cvijetićanin, N.; Nikolic, M.V. Looking into how nickel doping affects the structure, morphology, and optical properties of TiO_2 nanofibers. *Surf. Interfaces* **2024**, *49*, 104434. [CrossRef]
50. Xu, C.; Xiong, F.; Wang, Y.; Nai, J.; Zhang, W. Improving the intrinsic activity of ultrathin 2D–2D heterostructures by bridge-bonded Ni–O–Ti ligands for efficient oxygen evolution. *Nanotechnology* **2023**, *34*, 255402. [CrossRef]
51. Cui, E.; Li, Q.; Wang, X.; Xu, N.; Zhang, F.; Hou, G.; Xie, M.; Wang, Z.; Yang, X.; Zhang, Y. Regulating the interfacial electronic coupling of PtNi/TiO_2 via bond evolution for highly efficient hydrogenation of 5-hydroxymethylfurfural. *Appl. Catal. B Environ.* **2023**, *329*, 122560. [CrossRef]

Disclaimer/Publisher's Note: The statements, opinions and data contained in all publications are solely those of the individual author(s) and contributor(s) and not of MDPI and/or the editor(s). MDPI and/or the editor(s) disclaim responsibility for any injury to people or property resulting from any ideas, methods, instructions or products referred to in the content.